AGU PUBLICATIONS

Journal of Advances in Modeling Earth Systems

RESEARCH ARTICLE
10.1002/2017MS001083

Common Warming Pattern Emerges Irrespective of Forcing Location

Sarah M. Kang[1], Kiwoong Park[1], Fei-Fei Jin[2], and Malte F. Stuecker[3,4]

[1]School of Urban and Environmental Engineering, Ulsan National Institute of Science and Technology, Ulsan, South Korea, [2]Department of Atmospheric Sciences, SOEST, University of Hawai'i at Manoa, Honolulu, HI, USA, [3]Department of Atmospheric Sciences, University of Washington, Seattle, WA, USA, [4]Cooperative Programs for the Advancement of Earth System Science (CPAESS), University Corporation for Atmospheric Research (UCAR), Boulder, CO, USA

Abstract The Earth's climate is changing due to the existence of multiple radiative forcing agents. It is under question whether different forcing agents perturb the global climate in a distinct way. Previous studies have demonstrated the existence of similar climate response patterns in response to aerosol and greenhouse gas (GHG) forcings. In this study, the sensitivity of tropospheric temperature response patterns to surface heating distributions is assessed by forcing an atmospheric general circulation model coupled to an aquaplanet slab ocean with a wide range of possible forcing patterns. We show that a common climate pattern emerges in response to localized forcing at different locations. This pattern, characterized by enhanced warming in the tropical upper troposphere and the polar lower troposphere, resembles the historical trends from observations and models as well as the future projections. Atmospheric dynamics in combination with thermodynamic air-sea coupling are primarily responsible for shaping this pattern. Identifying this common pattern strengthens our confidence in the projected response to GHG and aerosols in complex climate models.

Key Points:
- Tropospheric warming pattern is insensitive to the location of surface heating
- The common warming pattern is characterized by enhanced warming in the tropical upper troposphere and the polar lower troposphere
- Excitation of common warming pattern is enabled by local air-sea interactions and internal atmospheric processes

Correspondence to:
S. M. Kang,
skang@unist.ac.kr

Citation:
Kang, S. M., Park, K., Jin, F.-F., & Stuecker, M. F. (2017). Common warming pattern emerges irrespective of forcing location. *Journal of Advances in Modeling Earth Systems*, *9*, 2413–2424. https://doi.org/10.1002/2017MS001083

Received 8 JUN 2017
Accepted 22 SEP 2017
Accepted article online 27 SEP 2017
Published online 27 OCT 2017

1. Introduction

Future climate change projections are complicated by the existence of multiple forcing agents such as CO_2, anthropogenic aerosols, ozone, land-use change, and ocean heat uptake. Forcing agents with the same magnitude of global mean radiative forcing but differing in their spatial pattern can elicit vastly different global mean surface temperature responses (Hansen et al., 1997, 2005). Hence, the concept of efficacy was introduced: a measure for the effectiveness of a forcing agent in warming the global surface relative to CO_2 forcing (Hansen et al., 2005; Winton et al., 2010). For example, forcings that project more strongly on the polar region exhibit greater efficacy (Forster et al., 2000; Kang & Xie, 2014; Rose et al., 2014). Marvel et al. (2016) showed that the efficacy of each forcing must be accounted for to better estimate the climate sensitivity. Other than the global mean surface warming, changes in column-integrated water vapor also depend significantly on the spatial pattern of radiative forcing (Rose & Rencurrel, 2016).

Despite the marked differences in the aforementioned climate responses induced by different forcings, a common tropospheric warming pattern can be recognized, which is characterized by an enhanced warming in the upper troposphere in the tropics and the lower troposphere in the polar region. Close investigations of zonal mean tropospheric temperature responses to various forcings such as changes of solar irradiance and atmospheric CO_2 concentration reveal this characteristic common warming pattern (Forster et al., 2000; Hansen et al., 1997, 2005). The same pattern emerges in historical temperature trends seen in the reanalysis data and the current generation of climate models (Xie et al., 2010, Figures 1a and 1b), with strong similarity to the response to a nearly uniform GHG increase in space (Figure 1c) and climate change projections under RCP8.5 (Figure 1d). All temperature trend patterns in Figure 1 exhibit (i) an enhanced warming in the tropical upper troposphere (Allen & Sherwood, 2008; Lorenz & DeWeaver, 2007) and (ii) pronounced surface warming in the polar region of almost twice the amplitude compared to the global average (referred to as Arctic or polar amplification) (Screen & Simmonds, 2010).

Ample evidence for global impacts to localized radiative forcing can serve as additional clues for the physical mechanisms behind the common warming pattern. For example, the climatic impact of aerosol forcing, which peaks in the northern hemisphere midlatitudes, exhibits global characteristics (Yoshimori & Broccoli,

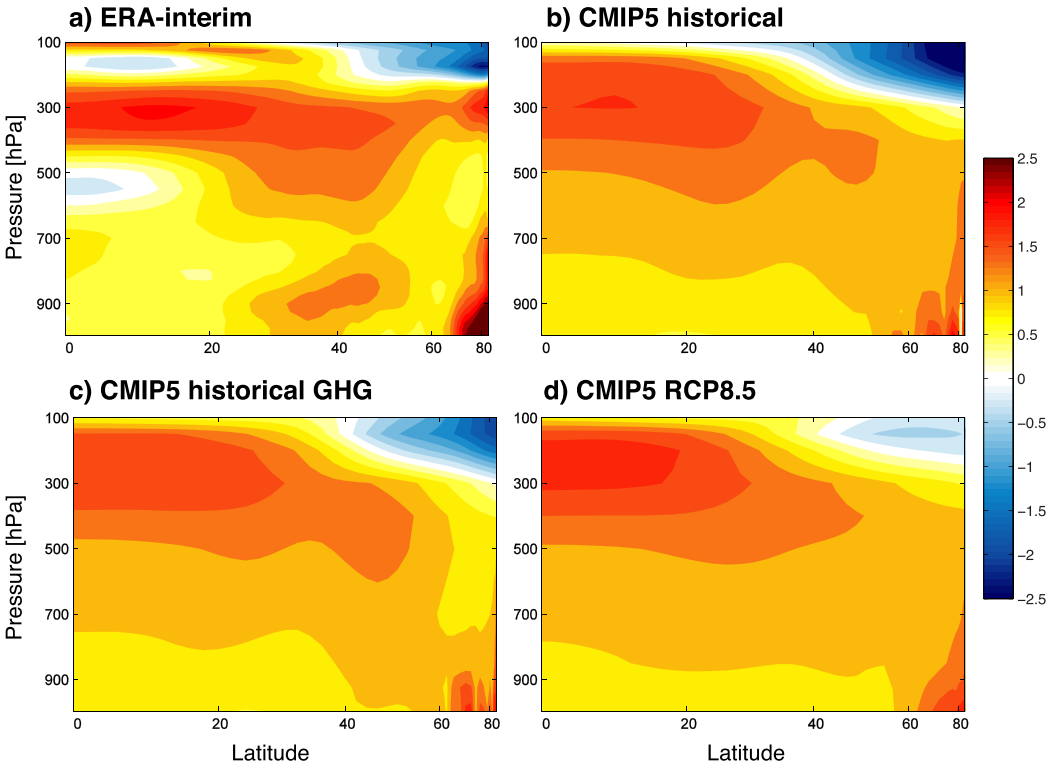

Figure 1. Hemispherically averaged linear trend of tropospheric temperature between 1979 and 2005 divided by the global mean of the skin temperature trend in: (a) ERA-Interim; (b) CMIP5 historical simulation ensemble mean; and (c) historical GHG simulation ensemble mean. (d) As in Figure 1b but for 2006–2100 in the CMIP5 RCP8.5 simulation ensemble mean. For all CMIP5 simulations, 18 models are selected for which historical GHG simulations are available (Table 1).

2008). The climate response pattern to a localized aerosol forcing shares a large commonality with that of a spatially uniform GHG forcing. The responses of surface air temperatures (Boer & Yu, 2003), sea surface temperatures (Xie et al., 2013), and precipitation (Xie et al., 2013) to GHG and aerosol forcing for the 20th century all resemble each other. Furthermore, the Asian summer monsoon change during the historical period under GHG and aerosol forcing also exhibits similar spatial patterns (Li et al., 2015). Finally, despite a large model spread in the patterns and magnitudes of radiative forcing among models (Zelinka et al., 2014), the surface temperature response in these models exhibits common features such as polar amplification (Serreze et al., 2009), peak equatorial warming (Xie et al., 2010), larger warming over land than ocean (Joshi et al., 2013), and muted warming signals in the Southern Ocean (Marshall et al., 2014) and North Atlantic (Drijfhout et al., 2012). Thus, a line of evidence suggests that the climate response patterns are largely insensitive to the forcing pattern.

Table 1
List of CMIP5 Models That are Used to Produce Figure 1

1	ACCESS1–3
2	bcc-csm1-1
3	BNU-ESM
4	CanESM2
5	CCSM4
6	CNRM-CM5
7	CSIRO-Mk3–6-0
8	FGOALS-g2
9	GFDL-CM3
10	GFDL-ESM2M
11	GISS-E2-H
12	GISS-E2-R
13	HadGEM2-ES
14	IPSL-CM5A-LR
15	MIROC-ESM
16	MIROC-ESM-CHEM
17	MRI-CGCM3
18	NorESM1-M

Earlier studies have demonstrated the possibility of a robust climate response pattern irrespective of forcing patterns—although indirectly—by contrasting single forcing simulations with GHG-only and aerosol forcing separately (Boer & Yu, 2003; Xie et al., 2013). To develop a comprehensive understanding of climate response pattern sensitivity to forcing patterns, one would ideally wish to assess it for as wide a range of forcing patterns as possible. Here, we develop a more complete picture of this sensitivity through a set of idealized model experiments that considers a wide range of possible surface heating distributions. We clearly demonstrate that a common tropospheric warming pattern emerges that is largely insensitive to the surface heating distribution.

2. Model Configuration and Experiment Setup

We use AM2.1, the atmospheric component of GFDL's CM2.1 model (Anderson et al., 2004; Delworth et al., 2006), with a horizontal resolution of 2° latitude by 2.5° longitude

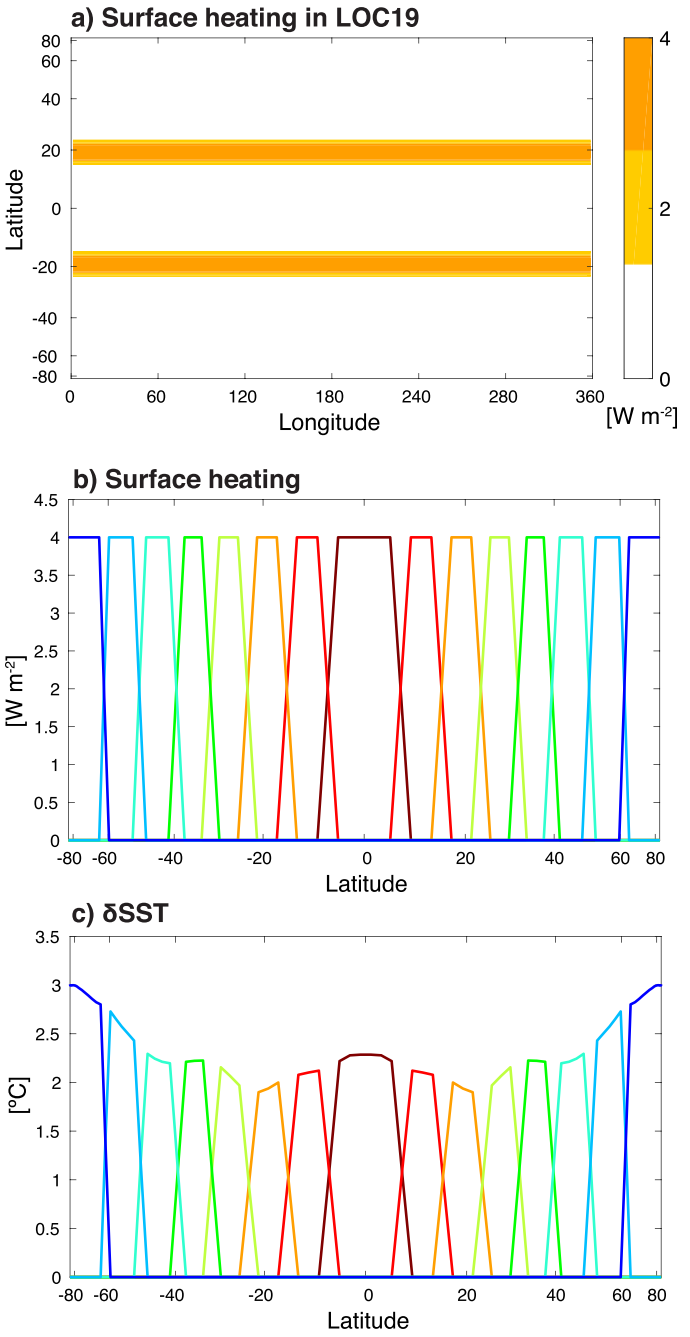

Figure 2. (a) An example of the prescribed surface heating distribution from the LOC19 experiment. (b) Zonal-mean of the prescribed surface heating distribution for all LOC experiments. (c) Profiles of the anomalous zonal-mean SST distribution in the fixed SST (F.SST) experiments.

and 24 vertical levels. The model is coupled to an aquaplanet slab ocean model for which sea surface temperatures (SSTs) are determined by the surface energy budget. The SSTs are permitted to drop below freezing temperatures without forming any sea ice, thus inhibiting the surface albedo feedback. The depth of the slab ocean is 50 m and the model is run under annual mean insolation with no diurnal cycle.

The reference climate with no surface flux adjustment (referred to as CNT) is perturbed by a zonally symmetric surface heat flux over a finite latitude band that is symmetric about the equator (Figure 2a). These perturbed experiments are denoted by the prefix LOC# where # denotes the center of the forced latitude band. Combining all individual experiments, the forced latitude bands span the whole globe from the equatorial region to the polar region (Figure 2b). The forcing patterns are constructed to have near zero correlation, as shown in Figure 3a below the diagonal. In total, eight LOC experiments are conducted. The globe is divided into eight bands so that the perturbed area in the experiment with the equatorial heating (LOC0) that encompasses the smallest number of grid points is still large enough to generate a robust and smooth climate signal, yet narrow enough to provide a high spatial resolution of the perturbations. The area of the forced latitude band in each case is constrained to be approximately identical to allow an equal comparison of the response to each LOC forcing. We perform these experiments with heating and cooling separately, with maximum amplitude of 4 Wm^{-2}, which amounts to the globally averaged forcing of $\sim$0.5 Wm^{-2}. The constant surface heating is linearly tapered to zero within two grid points at both lateral boundaries. The forcing of the sum of all LOC experiments is approximately analogous to a forcing from a doubling CO_2 experiment. We analyze the linear climate response component, which is obtained by the difference of the responses to heating and cooling divided by a factor of 2. All figures herein correspond to this linear climate response and the averages of the two hemispheres. CNT is integrated for 120 years and the average of last 100 years is analyzed. LOCs are branched out from CNT and are integrated for 60 years with the first 15 years discarded. This default model is referred to as FULL.

In section 4, we devise three additional experiments to unravel the mechanism for the common pattern formation. First, we inhibit cloud radiative effects (denoted as F.CRE). A randomly chosen 1 year time series (with 3 hourly temporal resolution) of the cloud water mixing ratio, cloud ice mixing ratio, and cloud fractional area extracted from FULL CNT are prescribed for both the control and the perturbed experiments (Kang et al., 2008). Second, we suppress the wind-evaporation-SST feedback (denoted as F.WES). The wind speed in the evaporation calculation for both the control and the perturbed experiments is prescribed to its time-mean and zonal-mean profile in FULL CNT (Kang et al., 2014). Third, we prescribe the sea surface temperatures (denoted as F.SST). To obtain the prescribed SST profile, we first compute the sum of the zonal-mean SST responses of all LOC experiments in FULL. This sum is then divided into eight finite latitude bands (Figure 2c), which are separately added to the time-mean SST profile in FULL CNT. Hence, the prescribed SST anomaly is associated with both localized and far-field effects of the surface fluxes. To examine the role of local air-sea interactions in exciting the common pattern, we intend to disregard SST anomalies outside of the forced latitude band. Instead, for any given latitude band, the local SST response of the corresponding LOC experiment and the remote SST responses for that location of the remaining LOC experiments are considered the forcing. A comparison of the sum of tropospheric temperature responses of

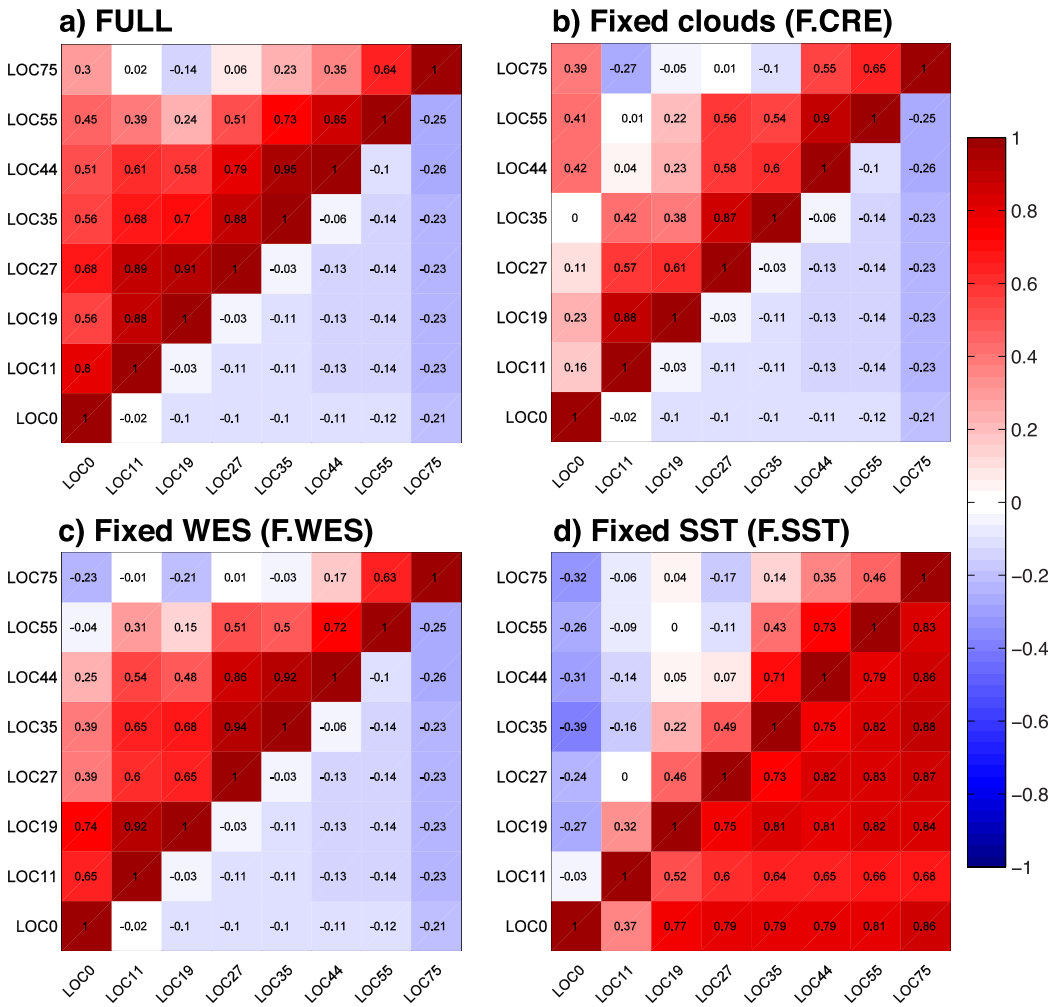

Figure 3. Values above the upper diagonal show the pattern correlation coefficients for the zonal-mean temperature response below 100 hPa between the different LOC experiments and values below the lower diagonal indicate the pattern correlation coefficients for the corresponding anomalous net surface heat fluxes in (a) the default experiment (FULL), (b) the fixed CRE experiment (F.CRE), (c) the inhibited WES experiment (F.WES), and (d) the fixed SST experiment (F.SST). The anomalous net surface heat fluxes in all models except F.SST correspond to the prescribed surface heating distribution in Figure 2.

all LOC experiments in FULL and F.SST will help enlighten the role of local air-sea interactions in setting the common tropospheric warming pattern since the SST responses are constructed to be identical. Both the control and the perturbed experiments with a modified model setting are branched out from FULL CNT and are integrated for 60 years with the first 15 years discarded.

3. Insensitivity of the Warming Pattern to Forcing Location

Figure 4 shows the tropospheric temperature response patterns for each LOC. A maximized warming in the midtroposphere shifts systematically poleward as the forcing shifts poleward. The surface warming response exhibits a local maximum that is colocated with the forcing location (Figure 5b). However, in all cases, the tropical response peaks in the upper troposphere near the tropopause, while the polar response is most prominent in the mid-to-lower troposphere. Also, the upper tropospheric temperature response in the tropics is horizontally homogeneous within 20° latitude. Note, however, the contrasting robustness of tropical and polar responses: the tropical response peaks in the upper troposphere in all cases while the polar response is less robust with a strong peak near the surface in LOC75 but with a modest peak in the midtroposphere in other cases. A detailed study of local and remote impacts of surface heating on polar amplification will be presented in a forthcoming study. The similarity of the tropospheric temperature

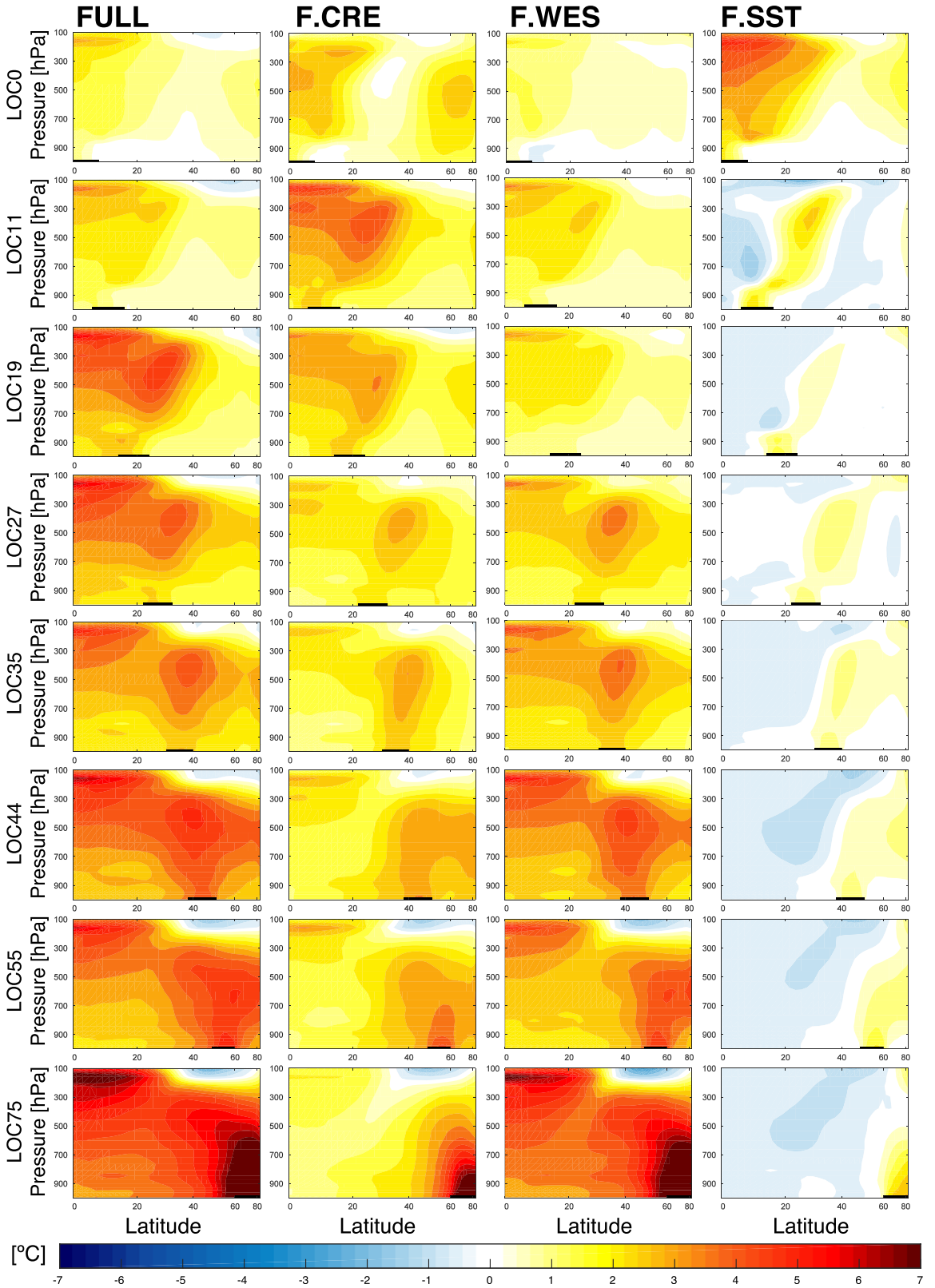

Figure 4. Time and zonal-mean tropospheric temperature response for each LOC in (first column) FULL, (second column) F.CRE, (third column) F.WES, and (fourth column) F.SST. The forced latitude bands are specified as black lines.

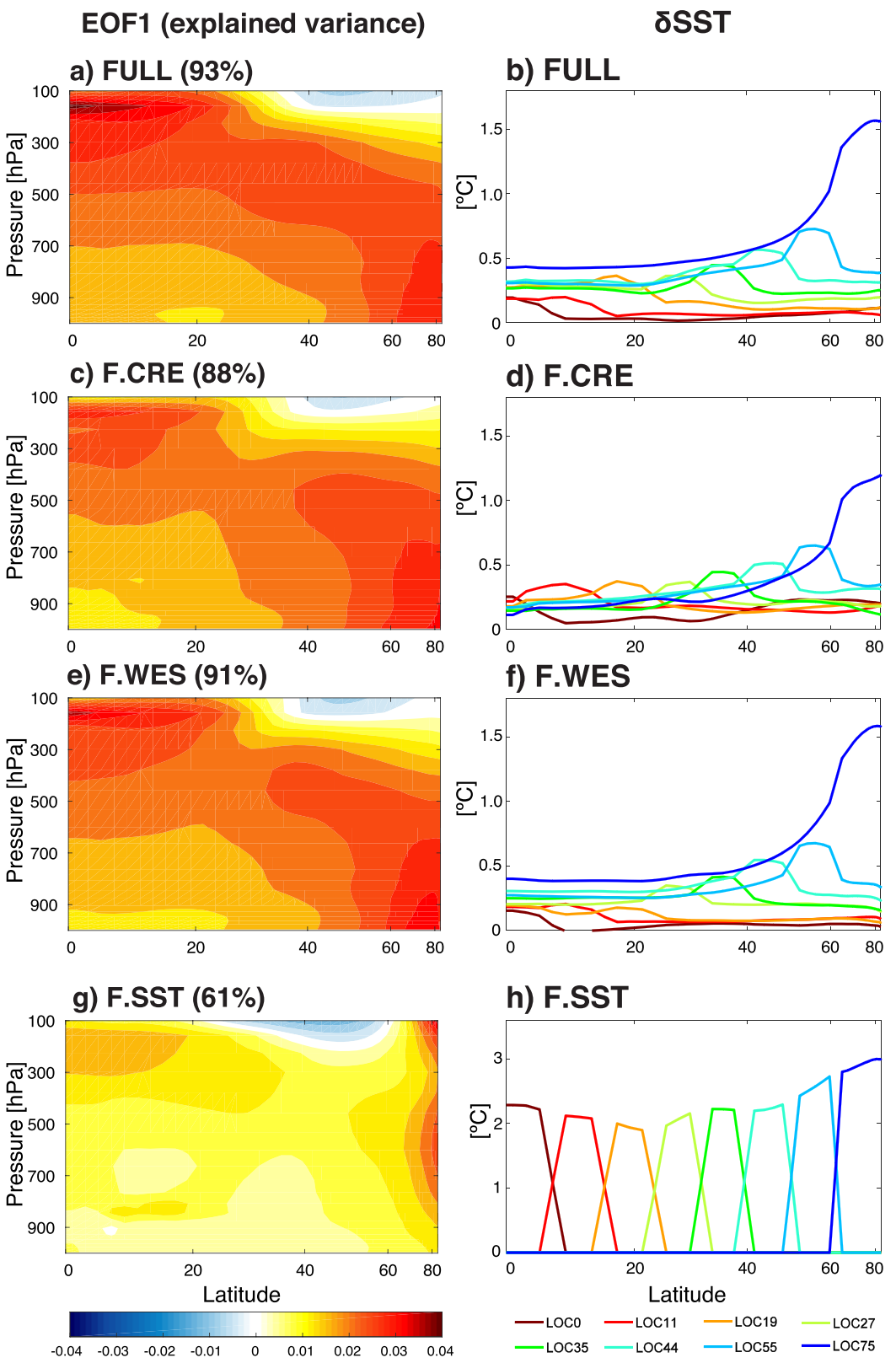

Figure 5. (left column) Leading EOF patterns (EOF1) for the zonal-mean temperature responses below 100 hPa with explained variance noted in brackets; right column, the zonal-mean SST response in all LOC experiments for: (a) and (b) the default experiment (FULL), (c) and (d) the fixed CRE experiment (F.CRE), (e) and (f) the inhibited WES experiment (F.WES), and (g) and (h), the fixed SST experiment (F.SST).

response patterns can be quantified by the spatial correlation coefficients between any two LOCs. The correlations for the zonal-mean tropospheric temperature response patterns (in pressure coordinates) below 100 hPa are displayed in Figure 3a above the diagonal. The values decay away from the diagonal, indicating that more similar response patterns emerge when the forcings between the two cases are located closer to each other. Overall the values are markedly greater than the negligibly small correlations between the corresponding forcing patterns (values below the diagonal in Figure 3a). For example, the linear correlation coefficient of the response patterns between LOC11 and LOC27 attains a value of 0.89, while it only attains a value of -0.11 for the respective forcing patterns. If the zonal-mean patterns are area-weighted by being multiplied by the square root of $\cos\varphi$ when computing the correlation coefficients, the less robust polar response pattern becomes de-emphasized so that the correlations of the tropospheric temperature response patterns systematically increase in all cases up to 0.2.

In contrast, the SST response peaks over the forced latitude band (Figure 5b), hence, the correlation coefficients of the SST responses are substantially lower than the corresponding values for the tropospheric temperature responses. For example, LOC27 and LOC35 exhibit a negligibly small correlation between their SST responses ($R = 0.14$), which is clearly contrasted by a large correlation between their tropospheric temperature responses ($R = 0.88$). This clearly suggests the existence of a common tropospheric temperature response pattern that is largely insensitive to the details of the surface heating distribution.

To identify this common pattern, we apply an empirical orthogonal function (EOF) analysis to the zonal-mean tropospheric temperature responses of all LOC experiments. Note that the EOF analysis is based on the covariance matrix of the zonal-mean tropospheric temperature responses (in pressure coordinates) below 100 hPa without area-weighting in order to capture the pattern changes in the polar region. The leading pattern (Figure 5a) explains 93% of the total variance and is characterized by a top-heavy warming in the tropics and a bottom-heavy warming in the polar region. The polar amplified pattern disappears when using the area-weighted covariance that puts more weight on the tropical pattern. Note the absence of active ocean dynamics in our experiments, implying that they are not essential for the pattern formation. Nevertheless, ocean dynamics should further modify and/or amplify this pattern, for instance by promoting a muted warming in the Southern Ocean and North Atlantic regions (Xie et al., 2013) or by amplifying the Arctic surface amplification pattern while reducing the midtropospheric Arctic warming (Singh et al., 2017). However, our results clearly demonstrate that atmospheric processes combined with a purely thermodynamic ocean adjustment alone are at work for the emergence of this common warming pattern.

How does this common temperature response pattern develop without ocean dynamics? One important reason is that atmospheric processes are effective at homogenizing the localized response. The SST response patterns (Figure 5b) to the localized surface forcing prominently show nonlocal effects due to thermodynamic ocean mixed layer adjustments. For instance, the global ocean surface is warmed most effectively in the polar forcing experiment (LOC75). It is interesting to note that the equatorial regions are warmed most effectively by polar forcing (LOC75) and least by local forcing (LOC0), consistent with results from earlier studies (Kang & Xie, 2014; Rose et al., 2014). Importantly, this implies that regional climate cannot be properly projected when only the information of local forcing is provided because remote forcing can have an even greater impact than local forcing for certain regions.

The local and remote effects for a given forcing are measured by the surface warming response over a given latitudinal band in each LOC experiment divided by its global sum (Figure 6a). By design, the sum of each row amounts to 100%. The diagonal component (solid lines in Figure 6d) indicates the fraction of local effects and the sum of the remainder in each row (dashed lines in Figure 6d) indicates the fraction of remote effects. The local effect amounts to only 20%–30% of the global response regardless of the forced latitude band. This value is close to the fraction expected from a completely diffusive climate system when the response becomes nearly isothermal, in which case the fraction of local effect is equal to the area fraction of the forced latitude band (12.5%). The large fraction of the remote effect of 70%–80% suggests that the forcing effect does not remain local. In particular, the local fraction increases as the forcing is shifted to higher latitudes. This is consistent with Rose et al. (2014) where the SST responses to high latitude forcings are more pronounced over the forced region whereas those to tropical forcings are nearly uniform.

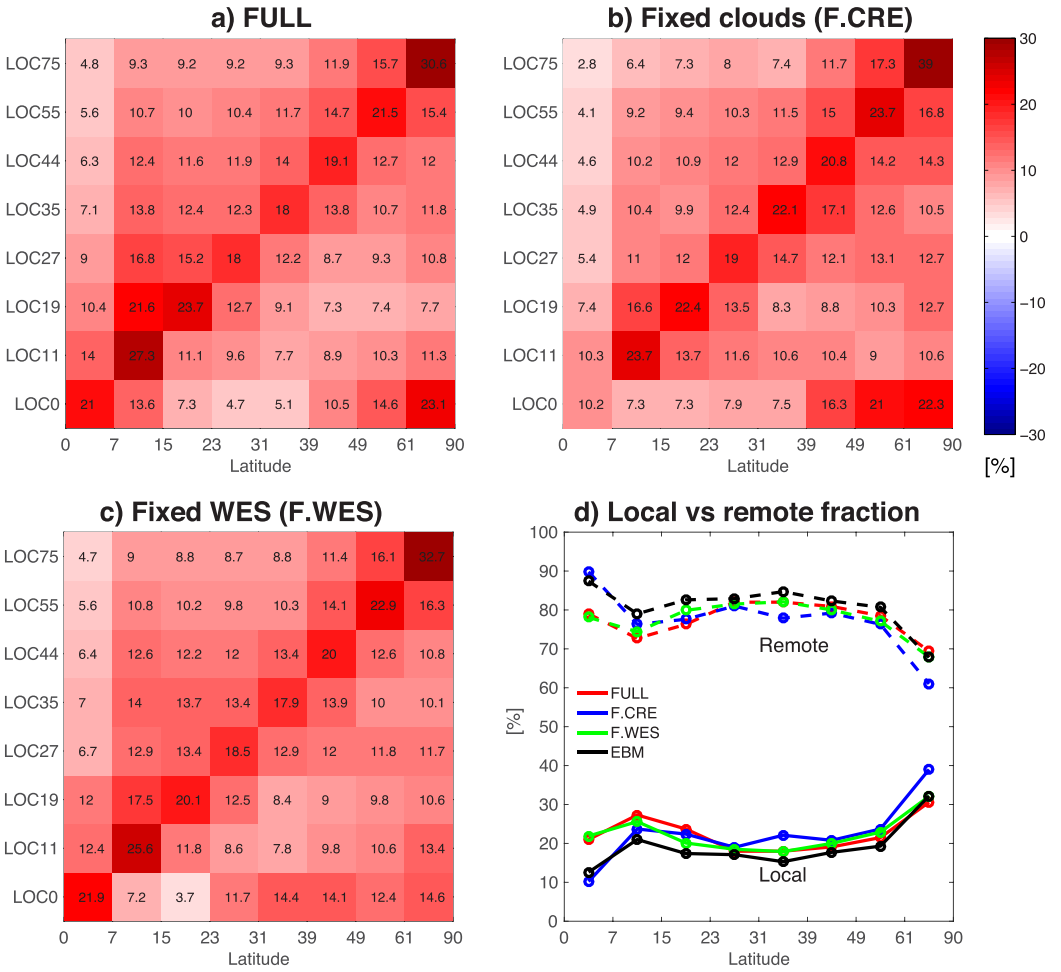

Figure 6. (a)–(c) Each row indicates the SST response in each latitude band divided by the globally integrated SST response for each LOC experiment in (a) the default experiment (FULL), (b) the fixed CRE experiment (F.CRE), and (c) the inhibited WES experiment (F.WES). (d) Local effect (diagonal component in Figures 6a–6c) in solid and remote effect (the sum of the remainder in each row in Figures 6a–6c) in dashed lines. Black lines in Figure 6d are from the diffusive EBM. Unit in percentage.

We invoke a diffusive one-dimensional energy balance model (EBM) to explain the large fraction of remote effects in response to a wide range of localized forcings. The atmospheric energy transport is assumed to be proportional to the latitudinal gradient of surface moist static energy $m=C_pT+Lq$, where T is the surface temperature (Hwang & Frierson, 2010; Kang et al., 2009; Rose et al., 2014). Hence, the top-of-atmosphere (TOA) energy budget can be written as:

$$\mathrm{SW}+\mathrm{LWCRF}-OLR_{clr}+H=-\frac{p_s}{g}D\nabla^2 m.$$

The left-hand side indicates the net atmospheric column energy and the right-hand side indicates the divergence of atmospheric energy transport. The clear-sky outgoing longwave radiation (OLR_{clr}) is linearized to be $aT-b$, with $a=2.57$ and $b=481.40$, calculated from a linear regression between their zonal-mean values of FULL CNT. We prescribe the zonal average of net TOA shortwave radiation (SW), longwave cloud radiative forcing (LWCRF), and net surface energy flux, which is the prescribed surface heating (H), from the perturbed LOC experiments. For reference, the total CRE response in FULL is shown in Figure 8. The diffusion coefficient D has a value of 1.05×10^6 m^2 s^{-1} everywhere, following Hwang and Frierson (2010), and the surface pressure is $p_s=9.8\times10^4$ Pa. The surface moist static energy m is calculated assuming 80% relative humidity. The surface temperature T is then predicted by the EBM from these inputs. The local and

remote fractions predicted from the EBM (black lines in Figure 6d) are close to the actual values in FULL (red lines in Figure 6d). These results are nearly unchanged if we use a different value for the diffusion coefficient, that is $D=1.6\times10^6$ m^2 s^{-1}. While the EBM represents a very simplified approximation of the climate system, it captures the large remote effect of localized surface heating as well as its dependence on the forcing location. As noted in Rose et al. (2014), a larger remote fraction (or a smaller local fraction) in the lower-latitude forcing cases is due to the stronger latitudinal gradient of background moisture that results in more efficient export of energy out of the tropics than in the higher-latitude forcing cases. The usefulness of the EBM in capturing the qualitative results from the general circulation model experiments implies that the SST response to localized forcing is likely spread globally by the communication between the extratropics and the Hadley circulation through diffusive eddy energy transport. The EBM results confirm that a climate system consisting of an atmosphere coupled to a thermodynamic slab ocean is very effective at spreading the effects of local surface forcing globally.

4. Mechanism of the Similar Pattern Formation

To unravel the dominant physical mechanism of the pattern formation, we conduct similar experiments as aforementioned, but with (1) inhibited cloud radiative effects (referred to as F.CRE), (2) suppressed wind-evaporation-SST (WES) feedback (referred to as F.WES), and (3) fixed SSTs (referred to as F.SST).

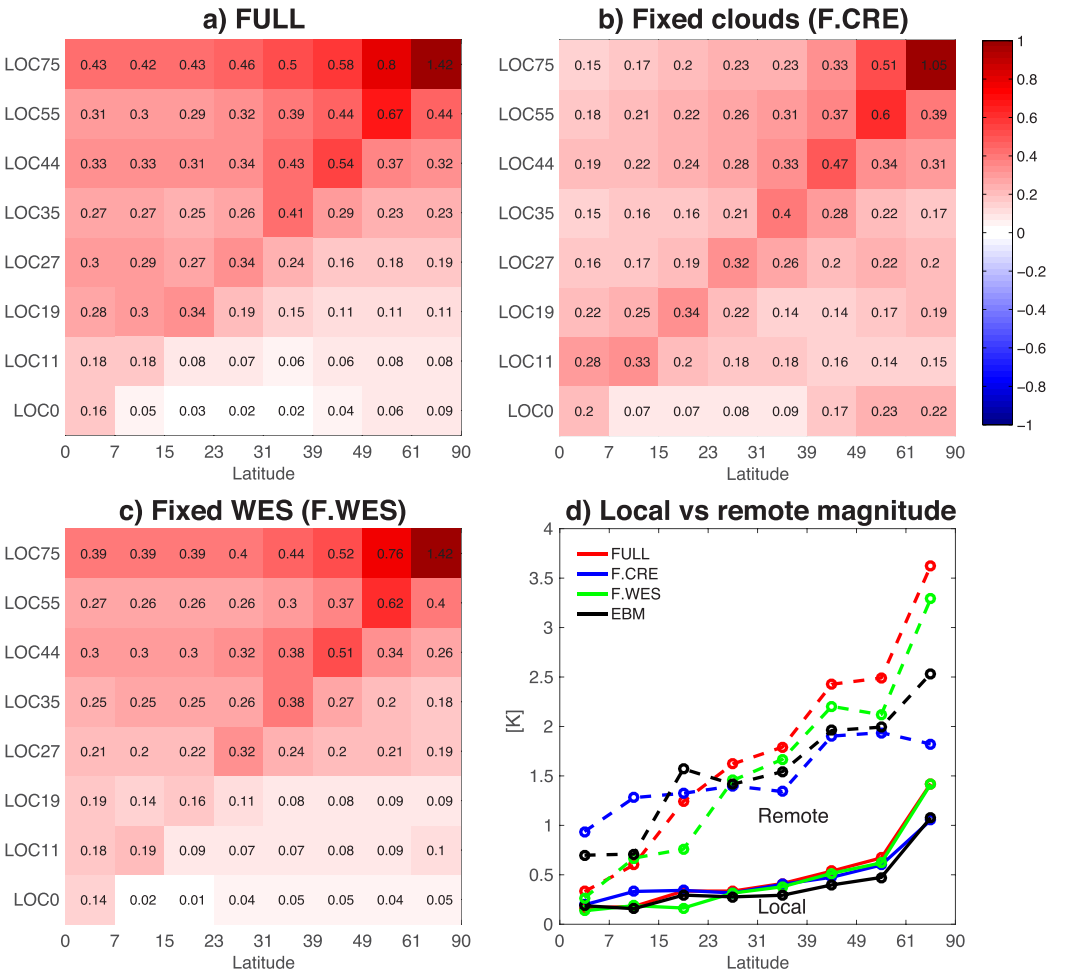

Figure 7. (a)–(c) Each row indicates the SST response in each latitude band for each LOC experiment in (a) the default experiment (FULL), (b) the fixed CRE experiment (F.CRE), and (c) the inhibited WES experiment (F.WES). (d) The SST response to local forcing (diagonal component in Figures 7a–7c) in solid and the SST response to remote forcing (the sum of the remainder in each row in Figures 7a–7c) in dashed lines. Black lines in Figure 7d are from the diffusive EBM.

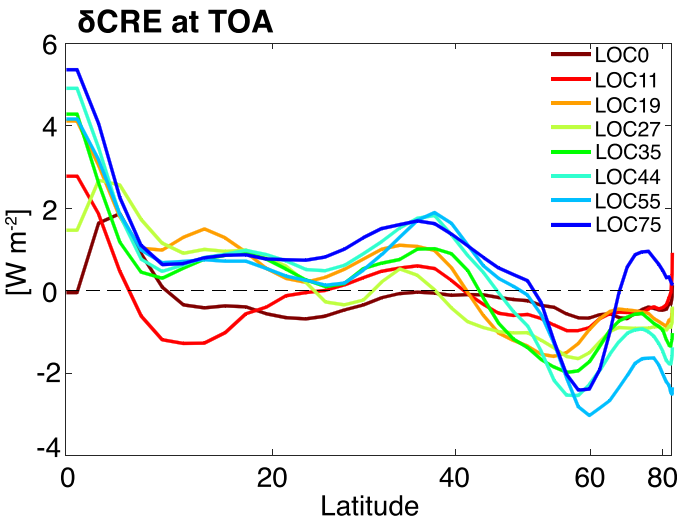

Figure 8. The zonal-mean response of top-of-atmosphere cloud radiative effects for all LOC experiments in FULL.

With inhibited cloud radiative effects (F.CRE), the spatial pattern of the leading mode of the temperature response remains similar to that in FULL (Figures 5a and 5c). However, the temperature response to subtropics-to-extratropical forcing (LOC19 and onward) is substantially diminished and localized compared to FULL (contrast first and second columns of Figure 4). The fraction of remote effects for these cases is slightly reduced as cloud radiative effects are inhibited (Figure 6d). In terms of the absolute magnitude, the dampening of the remote response amounts to 15%–50% reduction (Figure 7d). This can be understood from the zonal-mean CRE responses in FULL as shown in Figure 8. Most of the CRE responses can be attributed to the shortwave component (not shown). For the tropical forcing cases (LOC0 and LOC11), the CRE responses outside of the forcing location are negative due to an increase of low-level cloud amount in association with a strengthening of the Hadley cell. In contrast, positive CRE responses become systematically larger in the extratropics for the higher latitude forcing cases. Due to an absence of positive CRE in F.CRE, the remote responses for the subtropics-to-extratropical forcing cases become weaker, which in turn dampens the excitation of the common pattern. Indeed, the pattern correlations of the tropospheric temperature responses are significantly reduced from FULL to F.CRE (Figures 3a and 3b). Thus, we conclude that the cloud radiative effect contributes to the development of a common pattern, because in this model it serves as a strong positive feedback for forcings located outside of the equatorial region.

When SSTs are prescribed (F.SST), the tropospheric temperature responses become localized (fourth column of Figure 4). In general, the pattern correlation between any two LOC responses is significantly reduced despite fairly high correlations of the implied net surface heat fluxes (Figure 3d). A weak correlation for the temperature patterns emerges only with the neighboring forcing cases. The leading EOF pattern is distinct from that in FULL and F.CRE with no signature of polar amplification and its explained variance reduces significantly from 93% to 61% (Figure 5g). As a result, the sum of the tropospheric temperature responses of all LOC experiments in FULL and F.SST is markedly different, with a pattern correlation of only 0.15, despite identical SST responses. This illustrates an important role for local air-sea interactions in setting the common tropospheric warming pattern.

In contrast, when local air-sea interactions are allowed but WES feedback is suppressed (F.WES), the pattern correlation of the tropospheric temperature responses remains similar to that in FULL (contrast Figures 3a and 4c). The leading EOF pattern and its explained variance are also nearly unchanged (Figures 5a and 5e). Hence, when WES feedback is suppressed, the coupled system can find alternative ways to propagate the effect of localized forcing to remote regions, for example, through changes in the near-surface specific humidity (Mahajan et al., 2011). In the default model (FULL), WES feedback may still be an important process in setting up the common pattern, but it is not essential as suggested by the F.WES experiment. Thus, local air-sea interactions that allow remote SST changes are critical for the common pattern formation.

We propose the following mechanism for the common pattern formation. In the case of localized tropical forcing, its effect can be spread to remote regions by the Hadley circulation, while in the case of extratropical forcing its effect is communicated to remote regions via atmospheric eddies (Kang et al., 2009; Walker & Schneider, 2006). Positive cloud radiative effects that greatly amplify the temperature response both locally and remotely facilitate the propagation of the response to extratropical forcings. Furthermore, the effect of a local forcing can be spread on the surface via the WES feedback (Chiang & Bitz, 2005). When either local or remote forcings perturb the tropics, the temperature response will be amplified in the upper troposphere because the tropical atmosphere closely follows a moist adiabatic lapse rate. The tropical temperature response is then flattened within 20° latitude by fast equatorial wave adjustments (Sobel et al., 2002). As the atmospheric eddies perturb the polar region, the temperature response is amplified in the mid-to-lower troposphere due to large local static stability (Pithan & Mauritsen, 2014) and atmospheric energy transport (Graversen & Burtu, 2016). Therefore, any localized surface heating can excite a global response, enabled by local air-sea interactions and internal atmospheric processes that imprint characteristic patterns. Although

the SST response is a function of forcing pattern, any nonlocal SST response can excite a common warming pattern since the atmospheric response is mediated by surface heat fluxes regardless of the forcing location.

5. Conclusions

In this study, we utilize systematically designed idealized experiments with a comprehensive atmospheric general circulation model coupled to an aquaplanet slab ocean model for a wide range of surface heating distributions. Our results demonstrate that a common temperature response pattern exists regardless of the surface heating distribution (Figure 5a). This is consistent with earlier studies that emphasize the commonality of climate response patterns between aerosol and GHG forcing. However, local meridional temperature gradients exhibit a noticeable sensitivity to the surface heating distribution (Figures 4 and 5), which is important for determining atmospheric circulation changes through the thermal wind balance. Aerosol and GHG forcing also produce a distinctive meridional temperature structure, resulting in contrasting jet responses (Rotstayn et al., 2014). The SST response is also strongly shaped by the surface heating distribution due to changes in the local feedbacks (Rose et al., 2014). Nevertheless, the gross features of the tropospheric temperature response are surprisingly similar for a wide range of surface heating distributions that are virtually not correlated with each other.

The nonlocal SST responses enable an excitation of the common tropospheric warming pattern. We show that the cloud radiative effects in AM2 act to amplify the nonlocal effects of extratropical forcings, hence, assisting the excitation of the common pattern. In a multimodel study by Rose et al. (2014), AM2 exhibits by far the largest remote SST responses to localized forcing over high-latitudes as well as to localized forcing over the tropics. Moreover, it is AM2 that exhibits the most positive shortwave cloud radiative feedback. Thus, it is possible that AM2 may be particularly prone to emphasizing the common warming pattern. However, the physical mechanisms discussed here that are responsible for the common warming pattern should operate in any model, hence, the common warming pattern is expected to emerge but maybe to a lesser degree.

The identified common temperature response pattern exhibits remarkable similarities to the tropospheric temperature trends seen in the reanalysis (Figure 1a) and current generation of climate models for the historical period as well as the future projection (Figures 1b–1d). This pattern resembles those discussed in previous studies of historical trends from observations (Allen & Sherwood, 2008) and models (Thorne et al., 2011) as well as the future projections (Lorenz & DeWeaver, 2007). We emphasize that our idealized experimental setup exhibits sufficient realism to capture this pattern formation, while being simple enough to diagnose the individual fundamental dynamical processes that are responsible for its genesis. Our results suggest that the land-sea distribution and ocean dynamics are secondary for the development of the common temperature response pattern although they may amplify and/or modify it.

Acknowledgments
We thank two anonymous reviewers for their very constructive comments that greatly helped to improve an earlier version of the manuscript. We also thank Yen-Ting Hwang for sharing the Matlab code for the diffusive energy balance model. S.M.K. and K.P. were supported by Basic Science Research Program through the National Research Foundation of Korea (NRF) funded by the Ministry of Science, ICT and Future Planning (2016R1A1A3A04005520). M.F.S. was supported by the NOAA Climate and Global Change Postdoctoral Fellowship Program, administered by UCAR's Cooperative Programs for the Advancement of Earth System Sciences (CPAESS). The model data in this study can be obtained at https://github.com/UNISTkwpark/UNIST_CDL_COMMON_WARMING. In producing Figure 1, the ERA-interim data was obtained from http://apps.ecmwf.int/datasets/data/interim-full-mnth/ and the CMIP data were available at http://cmip-pcmdi.llnl.gov/cmip5/data_portal.html.

References

Allen, R. J., & Sherwood, S. C. (2008). Warming maximum in the tropical upper troposphere deduced from thermal winds. *Nature Geoscience*, *1*(6), 399–403. https://doi.org/10.1038/ngeo208

Anderson, J. L., Freidenreich, S. M., Garner, S. T., Gudgel, R. G., Gordon, C., & Held, I. M. (2004). The new GFDL global atmosphere and land model AM2–LM2: Evaluation with prescribed SST simulations. *Journal of Climate*, *17*(24), 4641–4673. https://doi.org/10.1175/JCLI-3223.1

Boer, G., & Yu, B. (2003). Climate sensitivity and response. *Climate Dynamics*, *20*(4), 415–429. https://doi.org/10.1007/s00382-002-0283-3

Chiang, J. C., & Bitz, C. M. (2005). Influence of high latitude ice cover on the marine intertropical convergence zone. *Climate Dynamics*, *25*(5), 477–496. https://doi.org/10.1007/s00382-005-0040-5

Delworth, T. L. Broccolib, A. J., Rosatia, A., Stouffera, R. J., Balajic, V., Beesleyd, J. A., . . . Zhang, R. (2006). GFDL's CM2 global coupled climate models. Part I: Formulation and simulation characteristics. *Journal of Climate*, *19*(5), 643–674. https://doi.org/10.1175/JCLI3629.1

Drijfhout, S., Van Oldenborgh, G. J., & Cimatoribus, A. (2012). Is a decline of AMOC causing the warming hole above the North Atlantic in observed and modeled warming patterns? *Journal of Climate*, *25*(24), 8373–8379. https://doi.org/10.1175/JCLI-D-12–00490.1

Forster, P. D. F., Blackburn, M., Glover, R., & Shine, K. (2000). An examination of climate sensitivity for idealized climate change experiments in an intermediate general circulation model. *Climate Dynamics*, *16*(10–11), 833–849. https://doi.org/10.1007/s003820000083

Graversen, R. G., & Burtu, M. (2016). Arctic amplification enhanced by latent energy transport of atmospheric planetary waves. *Quarterly Journal of the Royal Meteorological Society*, *142*(698), 2046–2054. https://doi.org/10.1002/qj.2802

Hansen, J., Sato, M., & Ruedy, R. (1997). Radiative forcing and climate response. *Journal of Geophysical Research*, *102*(D6), 6831–6864. https://doi.org/10.1029/96JD03436

Hansen, J., Sato, M., Ruedy, R., Nazarenko, L., Lacis, A., Schmidt, G. A., . . . Zhang, S. (2005). Efficacy of climate forcings. *Journal of Geophysical Research*, *110*, D18104. https://doi.org/10.1029/2005JD005776

Hwang, Y. T., & Frierson, D. M. (2010). Increasing atmospheric poleward energy transport with global warming. *Geophysical Research Letters*, *37*, L24807. https://doi.org/10.1029/2010GL045440

Joshi, M. M., Turner, A. G., & Hope, C. (2013). The use of the land-sea warming contrast under climate change to improve impact metrics. *Climatic Change*, *117*(4), 951–960. https://doi.org/10.1007/s10584-013-0715-6

Kang, S. M., Frierson, D. M., & Held, I. M. (2009). The tropical response to extratropical thermal forcing in an idealized GCM: The importance of radiative feedbacks and convective parameterization. *Journal of the Atmospheric Sciences*, *66*(9), 2812–2827. https://doi.org/10.1175/2009JAS2924.1

Kang, S. M., Held, I. M., Frierson, D. M., & Zhao, M. (2008). The response of the ITCZ to extratropical thermal forcing: Idealized slab-ocean experiments with a GCM. *Journal of Climate*, *21*(14), 3521–3532. https://doi.org/10.1175/2007JCLI2146.1

Kang, S. M., Held, I. M., & Xie, S.-P. (2014). Contrasting the tropical responses to zonally asymmetric extratropical and tropical thermal forcing. *Climate Dynamics*, *42*(7–8), 2033–2043. https://doi.org/10.1007/s00382-013-1863-0

Kang, S. M., & Xie, S.-P. (2014). Dependence of climate response on meridional structure of external thermal forcing. *Journal of Climate*, *27*(14), 5593–5600. https://doi.org/10.1175/JCLI-D-13–00622.1

Li, X., Ting, M., Li, C., & Henderson, N. (2015). Mechanisms of Asian summer monsoon changes in response to anthropogenic forcing in CMIP5 models. *Journal of Climate*, *28*(10), 4107–4125. https://doi.org/10.1175/JCLI-D-14–00559.1

Lorenz, D. J., & DeWeaver, E. T. (2007). Tropopause height and zonal wind response to global warming in the IPCC scenario integrations. *Journal of Geophysical Research*, *112*, D10119. https://doi.org/10.1029/2006JD008087

Mahajan, S., Saravanan, R., & Chang, P. (2011). The role of the wind–evaporation–sea surface temperature (WES) feedback as a thermodynamic pathway for the equatorward propagation of high-latitude sea ice–induced cold anomalies. *Journal of Climate*, *24*(5), 1350–1361. https://doi.org/10.1175/2010JCLI3455.1

Marshall, J., Armour, K. C., Scott, J. R., Kostov, Y., Hausmann, U., Ferreira, D., . . . Bitz, C. M. (2014). The ocean's role in polar climate change: Asymmetric Arctic and Antarctic responses to greenhouse gas and ozone forcing. *Philosophical Transactions of the Royal Society of London A: Mathematical, Physical and Engineering Sciences*, *372*(2019), 20130040. https://doi.org/10.1098/rsta.2013.0040

Marvel, K., Schmidt, G. A., Miller, R. L., & Nazarenko, L. S. (2016). Implications for climate sensitivity from the response to individual forcings. *Nature Climate Change*, *6*(4), 386–389. https://doi.org/10.1038/nclimate2888

Pithan, F., & Mauritsen, T. (2014). Arctic amplification dominated by temperature feedbacks in contemporary climate models. *Nature Geoscience*, *7*(3), 181–184. https://doi.org/10.1038/ngeo2071

Rose, B. E., Armour, K. C., Battisti, D. S., Feldl, N., & Koll, D. D. (2014). The dependence of transient climate sensitivity and radiative feedbacks on the spatial pattern of ocean heat uptake. *Geophysical Research Letters*, *41*, 1071–1078. https://doi.org/10.1002/2013GL058955

Rose, B. E., & Rencurrel, M. C. (2016). The vertical structure of tropospheric water vapor: Comparing radiative and ocean-driven climate changes. *Journal of Climate*, *29*(11), 4251–4268. https://doi.org/10.1175/JCLI-D-15–0482.1

Rotstayn, L. D., Plymin, E. L., Collier, M. A., Boucher, O., Dufresne, J.-L., Luo, J.-J., . . . Ming, Y. (2014). Declining aerosols in CMIP5 projections: Effects on atmospheric temperature structure and midlatitude jets. *Journal of Climate*, *27*(18), 6960–6977. https://doi.org/10.1175/JCLI-D-14–00258.1

Screen, J. A., & Simmonds, I. (2010). The central role of diminishing sea ice in recent Arctic temperature amplification. *Nature*, *464*(7293), 1334–1337. https://doi.org/10.1038/nature09051

Serreze, M., Barrett, A., Stroeve, J., Kindig, D., & Holland, M. (2009). The emergence of surface-based Arctic amplification. *The Cryosphere*, *3*(1), 11. https://doi.org/10.5194/tc-3–11-2009

Singh, H. A., Rasch, P. J., & Rose, B. E. J. (2017). Increased ocean heat convergence into the high latitudes with CO2-doubling enhances polar-amplified warming. *Geophysical Research Letters, 44.* https://doi.org/doi:10.1002/2017GL074561.

Sobel, A. H., Held, I. M., & Bretherton, C. S. (2002). The ENSO signal in tropical tropospheric temperature. *Journal of Climate*, *15*(18), 2702–2706. https://doi.org/10.1175/1520-0442(2002)015 < 2702:TESITT>2.0.CO;2

Thorne, P. W., Lanzante, J. R., Peterson, T. C., Seidel, D. J., & Shine, K. P. (2011). Tropospheric temperature trends: History of an ongoing controversy. *Wiley Interdisciplinary Reviews: Climate Change*, *2*(1), 66–88. https://doi.org/10.1002/wcc.80

Walker, C. C., & Schneider, T. (2006). Eddy influences on Hadley circulations: Simulations with an idealized GCM. *Journal of the Atmospheric Sciences*, *63*(12), 3333–3350. https://doi.org/10.1175/JAS3821.1

Winton, M., Takahashi, K., & Held, I. M. (2010). Importance of ocean heat uptake efficacy to transient climate change. *Journal of Climate*, *23*(9), 2333–2344. https://doi.org/10.1175/2009JCLI3139.1

Xie, S.-P., Deser, C., Vecchi, G. A., Ma, J., Teng, H., & Wittenberg, A. T. (2010). Global warming pattern formation: Sea surface temperature and rainfall. *Journal of Climate*, *23*(4), 966–986. https://doi.org/10.1175/2009JCLI3329.1

Xie, S.-P., Lu, B., & Xiang, B. (2013). Similar spatial patterns of climate responses to aerosol and greenhouse gas changes. *Nature Geoscience*, *6*(10), 828–832. https://doi.org/10.1038/ngeo1931

Yoshimori, M., & Broccoli, A. J. (2008). Equilibrium response of an atmosphere–mixed layer ocean model to different radiative forcing agents: Global and zonal mean response. *Journal of Climate*, *21*(17), 4399–4423. https://doi.org/10.1175/2008JCLI2172.1

Zelinka, M. D., Andrews, T., Forster, P. M., & Taylor, K. E. (2014). Quantifying components of aerosol-cloud-radiation interactions in climate models. *Journal of Geophysical Research: Atmospheres*, *119*, 7599–7615. https://doi.org/10.1002/2014JD021710